Journal of Science and Technology in Civil Engineering, HUCE, 2024, 18 (2): 113–129

STABILITY ANALYSIS OF A SQUARE TUNNEL IN COHESIVE-FRICTIONAL SOILS USING THE STABLE NODE-BASED SMOOTHED FINITE ELEMENT METHOD

Thien Vo-Minh[a,*]

[a]*Faculty of Civil Engineering, HUTECH University,*
475A, Dien Bien Phu street, Ward 25, Binh Thanh district, Ho Chi Minh City, Vietnam

Article history:
Received 17/7/2023, Revised 05/4/2024, Accepted 09/5/2024

Abstract

This paper presents a stable node-based smoothed finite element method (SNS-FEM) based on the upper theorem of limit analysis for stability analysis of a square tunnel in cohesive-frictional soils subjected to surcharge loading. The homogeneous soil is considered rigid-perfectly plastic and obeys the associated flow rule following the Mohr–Coulomb failure criterion. In this paper, the square tunnel is subjected to the surcharge loading σ_s on the ground surface. The variations of the stability number σ_s/c have been investigated for different values of the cover depth-to-width ratio of the tunnel H/B, unit weight $\gamma B/c$, and internal friction angle ϕ. Numerical results of square tunnels using the SNS-FEM approach demonstrate accuracy and efficiency. Design tables and charts of stability number results are provided for engineers to use in the preliminary design stage of the square tunnel.

Keywords: SNS-FEM; square tunnel; SOCP; upper bound limit analysis.

https://doi.org/10.31814/stce.huce2024-18(2)-09

1. Introduction

Rapid population growth has increased the demand for circular tunnels in transportation systems such as metros, highways, and railways. In recent years, square and rectangular tunnels have been widely used in subway stations, underground spaces, and mine tunnels. These tunnels are typically built in soils with cohesive and frictional properties. Therefore, this research aims to investigate the effects of surcharge loading on the stability analysis of square tunnels constructed in cohesive-frictional soils.

Numerous centrifuge model tests focusing on circular tunnels were conducted in the 1970s by researchers at the University of Cambridge, including works by Cairncross [1], Atkinson and Pott [2], and Seneviratne [3]. Later, Davis et al. [4], Mühlhaus [5], and Leca and Dormieux [6] used upper-bound rigid-block and lower-bound limit analysis to derive theoretical solutions for circular tunnel problems in cohesive-frictional soils. A limited study using the upper bound rigid-block method makes it difficult to postulate an admissible failure mechanism, especially for deeper tunnels and soils with high friction angles. The numbers and arrangement of the rigid blocks often limit the accuracy of this method and the ultimate failure mechanism. Then, Sloan and Assadi [7] first utilized finite element limit analysis (FELA) and linear optimization techniques to investigate the undrained stability of a square tunnel in cohesion soils. Highly efficient finite element limit analysis techniques, based on nonlinear optimization, Lyamin and Sloan [8] and Lyamin et al. [9] calculated the stability of circular and square tunnels in cohesive-frictional soils. Next, Yang and Yang [10] investigated the

*Corresponding author. *E-mail address:* vm.thien@hutech.edu.vn (T. Vo-Minh)

support pressure for a shallow rectangular tunnel in cohesive-frictional soil based on the upper bound rigid-block failure mechanisms. Recently, Yamamoto et al. [11, 12] used the finite element upper-bound and lower-bound theorem and nonlinear programming techniques to analyze the stability of circular and square tunnels in cohesive-frictional soils subjected to surcharge loading. More recently, Vo-Minh et al. [13] used the upper-bound limit analysis using the isogeometric analysis (IGA) and second-order cone programming (SOCP) optimization techniques to investigate the stability of circular tunnels in cohesive-frictional soils.

The finite element method (FEM) has recently gained significant popularity in various sciences and engineering fields. However, the standard FEM has inherent limitations and drawbacks, such as reduced accuracy when using lower-order elements, sensitivity to mesh distortion, and the occurrence of the volumetric locking phenomenon. To overcome these challenges, Liu et al. [14] introduced the node-based smoothed finite element method (NS-FEM) to address these drawbacks and analyze problems in solid mechanics using upper-bound solutions. The NS-FEM eliminates the volumetric locking by directly computing the strain smoothing associated with nodes using only the shape functions without coordinating transformation. Furthermore, the NS-FEM exhibits improved performance in highly distorted elements. It has been successfully applied to several engineering problems, including solid mechanics (Nguyen-Thoi et al. [15, 16], and limit analysis of solid problems [17]. A few years ago, Vo-Minh et al. [18–20] utilized the NS-FEM with the upper bound limit analysis theorem to examine the stability of tunnels in cohesive-frictional soils. Recently, Vo-Minh [21] employed the NS-FEM and SOCP for slope stability analysis in cohesive-frictional soils.

For dynamic structural analysis and acoustic problems, the NS-FEM has been found to have limitations due to its inherent "overly-soft" nature, which leads to temporal instability. Various numerical improvements have been proposed to address this issue in recent years. For example, Liu et al. [22] introduced the α-FEM, a combination of the FEM and the NS-FEM with an adjustable stabilization parameter α, while Xu et al. [23] presented the hybrid smoothed finite element method (H-SFEM). However, these methods require an uncertain parameter α, making calculation results highly sensitive to its value. To overcome the need for an uncertain parameter α, Wang et al. [24] introduced the stable node-based smoothed finite element method (SNS-FEM) for the analysis of 2D acoustic problems. The SNS-FEM utilizes the smoothing domain associated with nodes from the NS-FEM and expands the smoothed shape function gradient using the first-order Taylor equation in an approximation integral domain. Additionally, six extra integration points (for 3D space) or four additional integration points (for 2D space) are introduced to modify the smoothed strain. The SNS-FEM has been successfully applied in various fields, including static and dynamic analysis of solid mechanics (Feng et al. [25]) and metal forming problems (Yang et al. [26]). Recently, Vo-Minh and Nguyen-Son [27] employed the SNS-FEM based on the upper-bound limit analysis to evaluate the stability of two circular tunnels at different depths. More recently, Vo-Minh and Nguyen [28], and Vo-Minh et al. [29] investigated the seismic stability of a circular and a square tunnel in cohesive-frictional soils using the SNS-FEM.

This research paper aims to apply the SNS-FEM and SOCP optimization for stability analysis of a square tunnel in cohesive-frictional soils subjected to surcharge loading. To confirm the validity and accuracy of the SNS-FEM method, the stability numbers of a square tunnel are compared with the average values of the lower and upper bound using FELA and nonlinear optimization techniques reported by Yamamoto et al. [12]. The authors used low-order triangular elements and velocity discontinuities to maintain the numerical accuracy in their approaches. The key idea of the proposed method SNS-FEM is that the strain field within the smoothing domain is not a smoothed constant but

varies linearly, effectively overcoming the overly soft problem of the NS-FEM and temporal instability. Furthermore, the Mohr–Coulomb yield criterion can be formed in a SOCP using the SNS-FEM. The problem can be solved by the primal-dual interior-point method implemented in the Mosek software package [30]. This algorithm proved to be an effective optimization tool for limit analysis in geotechnical engineering.

The paper is organized as follows: Section 2 describes the problem definition. Section 3 briefly overviews the upper bound limit analysis formulation based on the SNS-FEM method. Numerical examples of stability analysis for a square tunnel are presented and discussed in Section 4. Finally, some concluding remarks are made in Section 5.

2. Problem definition

The plane strain square tunnel model has width B, cover depth H, and is subjected to the ultimate surcharge loading σ_s on the ground surface, as shown in Fig. 1. The boundary of the problem is chosen sufficiently distance away from the tunnel periphery, which has a width $2L$ and a height $H + B + h$. In this study, to eliminate the boundary effects of the domain, the values of $L = 3B - 7B$, $H = B - 5B$, and $h = B - 2B$ are assumed to be sufficiently large, and the failure mechanisms are inside the problem. The soil behavior is described as homogeneous Mohr–Coulomb material with cohesion c, friction angle ϕ and unit weight γ, and drained loading conditions are assumed. In this study, a dimensionless stability number σ_s/c is defined by using a functional relationship of $\phi, \gamma B/c$ and H/B are given as

$$\frac{\sigma_s}{c} = f\left(\frac{H}{B}, \frac{\gamma B}{c}, \phi\right) \tag{1}$$

This paper considers the tunnel ratio of cover depth and the width of the square tunnel H/B = 1-5. The dimensionless unit weight $\gamma B/c$ ranges from 0 to 2, and the value of soil friction angle ϕ varies from 0° to 35° is investigated. The horizontal displacements are free ($u \neq 0$) or fixing ($u = 0$) along the ground surface to describe the smooth or rough interface condition between the soil and the surcharge loading. The limitation of this study is that it does not consider the initial stress and the effect of the groundwater surrounding a square tunnel.

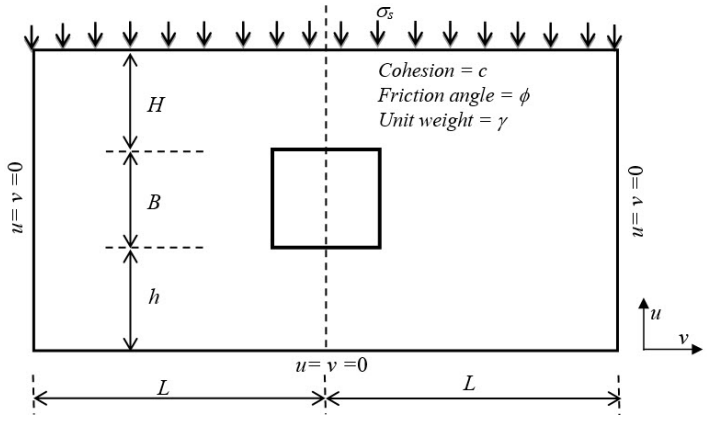

Figure 1. Square tunnel subjected to surcharge loading

3. Upper bound limit analysis in the geomechanics problem using a stable node-based smoothed finite element method (SNS-FEM)

3.1. The upper bound limit analysis for plane strain in geotechnical problems

Under the assumption of small deformation, a two-dimensional problem domain Ω bounded by a continuous boundary $\Gamma_{\dot{\mathbf{u}}} \cup \Gamma_{\mathbf{t}} = \Gamma, \Gamma_{\dot{\mathbf{u}}} \cap \Gamma_{\mathbf{t}} = \varnothing$ is considered. Assumed that the domain is subjected

to body forces $\mathbf{f}$ and external tractions $\mathbf{g}$ on the Neumann boundary $\Gamma_{\mathbf{t}}$, while the velocity vector $\dot{\mathbf{u}} = [\ \dot{u} \quad \dot{v}\ ]^T$ prescribes the Dirichlet boundary $\Gamma_{\dot{\mathbf{u}}}$.

The upper bound theorem indicates that a structure is expected to collapse when there exists a kinematically admissible velocity field for which the external work rate $W_{ext}(\dot{\mathbf{u}})$ is greater than the internal plastic dissipation rate $W_{int}(\sigma, \dot{\mathbf{u}})$ such that

$$W_{int}(\boldsymbol{\sigma}, \dot{\mathbf{u}}) < W_{ext}(\dot{\mathbf{u}}) \tag{2}$$

where

$$\begin{cases} W_{int}(\boldsymbol{\sigma}, \dot{\mathbf{u}}) = \displaystyle\int_{\Omega} D_p(\dot{\mathbf{u}}) d\Omega = \int_{\Omega} \boldsymbol{\sigma}\dot{\boldsymbol{\varepsilon}} d\Omega \\ W_{ext}(\dot{\mathbf{u}}) = \displaystyle\int_{\Omega} \mathbf{f}\dot{\mathbf{u}} d\Omega + \int_{\Gamma_t} \mathbf{g}\dot{\mathbf{u}} d\Gamma \\ \dot{\boldsymbol{\varepsilon}} = \left[\ \dot{\varepsilon}_{xx} \quad \dot{\varepsilon}_{yy} \quad \dot{\gamma}_{xy}\ \right]^T = \nabla\dot{\mathbf{u}} \\ U = \left\{ \dot{\mathbf{u}} : \dot{\mathbf{u}} = \dot{\mathbf{u}}_0 \quad \text{on } \Gamma_{\dot{\mathbf{u}}}, W_{ext}(\dot{\mathbf{u}}) > 0 \ \right\} \\ \boldsymbol{\sigma} \in \{\boldsymbol{\sigma} : \psi(\boldsymbol{\sigma}) \le 0\} \end{cases} \tag{3}$$

$\dot{\mathbf{u}}$ and $\boldsymbol{\sigma}$ denote the kinematically admissible velocity field and plastically admissible stress, respectively; $\psi(\boldsymbol{\sigma})$ is the yield function.

In the upper bound limit analysis, plastic dissipation can be expressed

$$W_{int}(\boldsymbol{\sigma}, \dot{\mathbf{u}}) = \alpha^+ W_{ext}(\dot{\mathbf{u}}), \forall \dot{\mathbf{u}} \in U \tag{4}$$

where α^+ is the collapse load multiplier.

Setting $C = \{\dot{\mathbf{u}} \in U | W_{ext}(\dot{\mathbf{u}}) = 1\}$, the collapse multiplier α^+ can be determined from the following optimization problem

$$\begin{aligned} \alpha^+ &= \max\left\{ \exists \boldsymbol{\sigma} \in \sum | W_{int}(\boldsymbol{\sigma}, \dot{\mathbf{u}}) = \alpha^+ W_{ext}(\dot{\mathbf{u}}), \forall \dot{\mathbf{u}} \in U \right\} = \min_{\dot{\mathbf{u}} \in U} D_p(\dot{\mathbf{u}}) \\ st &\begin{cases} \dot{\mathbf{u}} = 0 \quad \text{on } \Gamma_u \\ W_{ext}(\dot{\mathbf{u}}) = \displaystyle\int_{\Omega} \mathbf{f}\dot{\mathbf{u}} d\Omega + \int_{\Gamma_t} \mathbf{g}\dot{\mathbf{u}} d\Gamma = 1 \end{cases} \end{aligned} \tag{5}$$

In geotechnical problems, the soil is considered rigid-perfectly plastic and obeys the associated flow rule following the Mohr–Coulomb failure criterion. The internal plastic dissipation equation for plane strain conditions is proposed by Makrodimopoulos and Martin [31] as follows

$$D_p(\dot{\mathbf{u}}) = c\cos\phi \int_{\Omega} \sqrt{\dot{\boldsymbol{\varepsilon}}^T \Theta \dot{\boldsymbol{\varepsilon}}} d\Omega \text{ with } \dot{\boldsymbol{\varepsilon}} = \left[\ \dot{\varepsilon}_{xx} \quad \dot{\varepsilon}_{yy} \quad \dot{\gamma}_{xy}\ \right]^T \text{ and } \Theta = \begin{bmatrix} 1 & -1 & 0 \\ -1 & 1 & 0 \\ 0 & 0 & 1 \end{bmatrix} \tag{6}$$

where ϕ is the friction angle and c is the soil cohesion.

3.2. A brief of a stable node-based smoothed finite element method (SNS-FEM)

This section briefly describes a stable node-based smoothed finite element method (SNS-FEM) presented by Feng et al. [25].

The problem domain Ω is subdivided into non-overlapping and non-gap smoothing domains based on the background cells, with the condition that $\Omega = \sum_{k=1}^{N_n} \Omega_k^s$ and $\Omega_i^s \cap \Omega_j^s = \varnothing, i \neq j$, where N_n denotes the total number of field nodes. Fig. 2(a) shows how a nodal smoothing domain Ω_k^s associated with node k is constructed by connecting the mid-edge points to the centroid of surrounding triangular elements. The boundary of the smoothing domain Ω_k^s is labeled as Γ_k, and the union of all Ω_k^s forms the entire problem domain Ω.

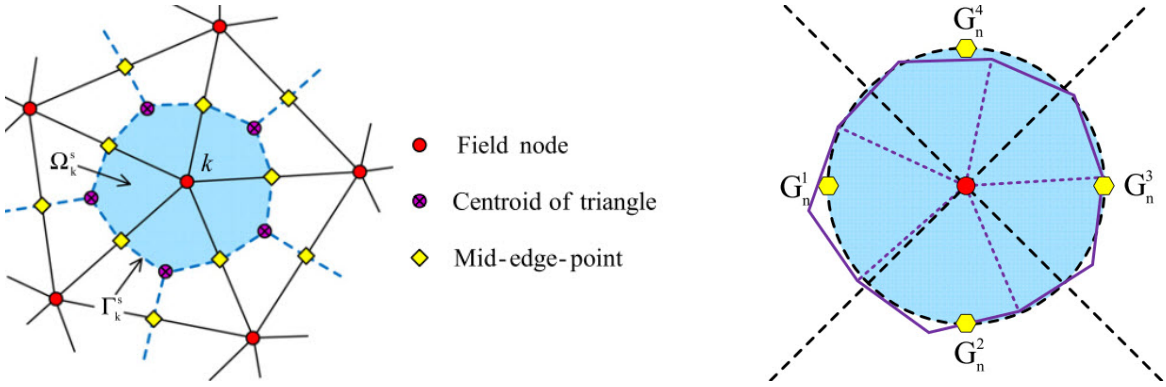

(a) The smoothing cells associated with the node k

(b) The approximate integration domain and integration points for SNS-FEM

Figure 2. The schematic of a node-based smoothing domain for node k

Using the NS-FEM, Liu et al. [14] calculated the smoothed strain rates on the cell Ω_k^s associated with node k as follows

$$\tilde{\dot{\boldsymbol{\varepsilon}}}_k = \sum_{k \in N^{(s)}} \tilde{\mathbf{B}}_k(\mathbf{x}_s)\mathbf{d}_k \tag{7}$$

where $N^{(s)}$ is the set containing nodes directly connected to node k, $\mathbf{d}_k$ is the nodal displacement vector and $\tilde{\mathbf{B}}_k(\mathbf{x}_s)$ is a smoothed strain-displacement matrix given by

$$\tilde{\mathbf{B}}_k(\mathbf{x}_s) = \begin{bmatrix} \tilde{b}_{kx}(x_s) & 0 \\ 0 & \tilde{b}_{ky}(x_s) \\ \tilde{b}_{ky}(x_s) & \tilde{b}_{kx}(x_s) \end{bmatrix} \tag{8}$$

where

$$\tilde{b}_{kh}(x_s) = \frac{1}{A_k^{(s)}} \int_{\Gamma_k} \mathbf{n}_h^{(s)}(\mathbf{x})\mathbf{N}_k(\mathbf{x})\mathrm{d}\Gamma = \frac{1}{A_k^{(s)}} \sum_{k=1}^{M} \mathbf{N}_k(\mathbf{x}_k^{GP}) n_{kh}^{(s)} l_k^{(s)}, (h = x, y) \tag{9}$$

where $A_k^{(s)} = \int_{\Omega_k^s} d\Omega$ is the area of the cell Ω_k^s, $N_{(k)}(\mathbf{x})$ is the FEM shape function for node k, and $\mathbf{n}^{(s)}(\mathbf{x})$ is the normal outward vector on the boundary $\Gamma_k^{(s)}$, M is the number of the sub-boundary of $\Gamma_k^{(s)}$. The Gauss point of $\Gamma_k^{(s)}$ is $\mathbf{x}_k^{GP}$, which has length $l_k^{(s)}$ and outward unit normal $n_{kh}^{(s)}$.

The SNS-FEM approach utilizes a node-based strain smoothing technique, employing linear strain fields over the smoothed domain on 3-node triangular elements. To establish a stable node smooth domain Ω_k^{sc}, an integral region formed by all the element domains of node k is approximated to a

circle with the same area. Subsequently, the smooth domain Ω_k^s is divided into four subdomains to obtain four integration points $G_n^i (i = 1, 2, 3, 4)$, as shown in Fig. 2(b).

The radius of the equivalent circle is defined by

$$r_c = \sqrt{\frac{A_k^s}{\pi}} \tag{10}$$

where $A_k^{(s)}$ is the area of the cell Ω_k^s.

Feng et al. [25] proposed that the smoothed strain in an approximation integral domain is expanded at the first order of the Taylor equation

$$\tilde{\dot{\boldsymbol{\varepsilon}}} = \tilde{\dot{\boldsymbol{\varepsilon}}}_k + \frac{\partial \tilde{\dot{\boldsymbol{\varepsilon}}}}{\partial x}(x - x_k) + \frac{\partial \tilde{\dot{\boldsymbol{\varepsilon}}}}{\partial y}(y - y_k) \tag{11}$$

Therefore, the smoothed strains of the four domains $\tilde{\dot{\boldsymbol{\varepsilon}}}_1^{sc}, \tilde{\dot{\boldsymbol{\varepsilon}}}_2^{sc}, \tilde{\dot{\boldsymbol{\varepsilon}}}_3^{sc}, \tilde{\dot{\boldsymbol{\varepsilon}}}_4^{sc}$ are

$$\tilde{\dot{\boldsymbol{\varepsilon}}}_1^{sc} = \tilde{\dot{\boldsymbol{\varepsilon}}}_k - \frac{\partial \tilde{\dot{\boldsymbol{\varepsilon}}}}{\partial x} r_c; \quad \tilde{\dot{\boldsymbol{\varepsilon}}}_2^{sc} = \tilde{\dot{\boldsymbol{\varepsilon}}}_k - \frac{\partial \tilde{\dot{\boldsymbol{\varepsilon}}}}{\partial y} r_c; \quad \tilde{\dot{\boldsymbol{\varepsilon}}}_3^{sc} = \tilde{\dot{\boldsymbol{\varepsilon}}}_k + \frac{\partial \tilde{\dot{\boldsymbol{\varepsilon}}}}{\partial x} r_c; \quad \tilde{\dot{\boldsymbol{\varepsilon}}}_4^{sc} = \tilde{\dot{\boldsymbol{\varepsilon}}}_k + \frac{\partial \tilde{\dot{\boldsymbol{\varepsilon}}}}{\partial y} r_c \tag{12}$$

Using the SNS-FEM, a smoothing strain around node k can be modified following Eq. (12) for the 2D problem

$$\widehat{\dot{\boldsymbol{\varepsilon}}}_k = \tilde{\dot{\boldsymbol{\varepsilon}}}_k + (\tilde{\dot{\boldsymbol{\varepsilon}}}_k^{sc})_x^T (\tilde{\dot{\boldsymbol{\varepsilon}}}_k^{sc})_x \frac{A_k^s}{2} + (\tilde{\dot{\boldsymbol{\varepsilon}}}_k^{sc})_y^T (\tilde{\dot{\boldsymbol{\varepsilon}}}_k^{sc})_y \frac{A_k^s}{2} \tag{13}$$

Noting that the four additional points in the SNS-FEM are just temporary variables, the original NS-FEM code is revised with only slightly modified.

In geotechnical problems, the domain is discretized by N_e triangular elements and the total nodes N_n. Substituting the stable smoothed strains rates vector $\widehat{\dot{\boldsymbol{\varepsilon}}}$ in Eq. (13) into Eq. (5), the upper-bound limit analysis using the SNS-FEM in plane strain geotechnical problems can be written

$$\alpha^+ = \frac{\sigma_s}{c} = \min\left(\sum_{i=1}^{N_n} cA_i \cos\phi \sqrt{(\widehat{\dot{\varepsilon}}_{xx}^i - \widehat{\dot{\varepsilon}}_{yy}^i)^2 + (\widehat{\dot{\gamma}}_{xy}^i)^2}\right) = \min\left(\sum_{i=1}^{N_n} cA_i t_i \cos\phi\right)$$

$$\text{s.t} \begin{cases} t_i \geq \sqrt{(\widehat{\dot{\varepsilon}}_{xx}^i - \widehat{\dot{\varepsilon}}_{yy}^i)^2 + (\widehat{\dot{\gamma}}_{xy}^i)^2}, \; i = 1, 2, \ldots, N_n \\ \dot{u} \neq 0, \;\; \dot{v} = \text{const} \quad \text{on } \Gamma_t \; (\textit{smooth}) \\ \dot{u} = 0, \;\; \dot{v} = \text{const} \quad \text{on } \Gamma_t \; (\textit{rough}) \\ \dot{\mathbf{u}} = 0 \quad \text{on } \Gamma_{\mathbf{u}} \\ W_{ext}(\dot{\mathbf{u}}) = 1 \\ \widehat{\dot{\varepsilon}}_{xx}^i + \widehat{\dot{\varepsilon}}_{yy} = t_i \sin\phi \end{cases} \tag{14}$$

where α^+ is a stability number, N_n is the total number of nodes in the domain, A_i is the area of node i, t_i is the additional variable, c is the cohesion value, and ϕ is the friction angle of the soil. The first constraint in Eq. (14) is a form of SOCP optimization. The upper bound limit analysis based on the SNS-FEM approach and SOCP has been implemented in Matlab. The conic interior-point optimizer of the academic Mosek package [30] is utilized to solve geotechnical engineering problems.

4. Numerical examples

Due to the symmetry of the problem, only half of a square tunnel was used in the upper bound simulation. The numerical analysis employed typical finite element meshes consisting of 3477 triangular elements for the case $H/B = 1$, which were used to generate the deformed shape and velocity plots shown in Fig. 3. GiD [32] software was utilized to create triangular elements for the square tunnel. The domain size was assumed to be large enough to eliminate the boundary effects, and the plastic zones were contained entirely within the domain.

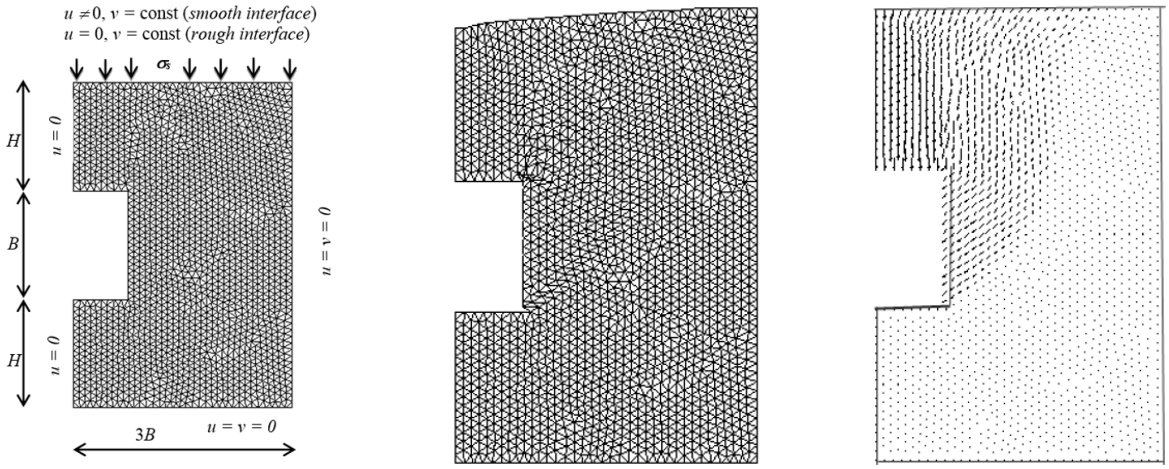

(a) Typical mesh (b) Deformed shape (c) Velocity plot

Figure 3. Typical finite element mesh for a square tunnel in the case $H/B = 1$, $\gamma B/c = 1, \phi = 5°$

4.1. Results of failure mechanisms

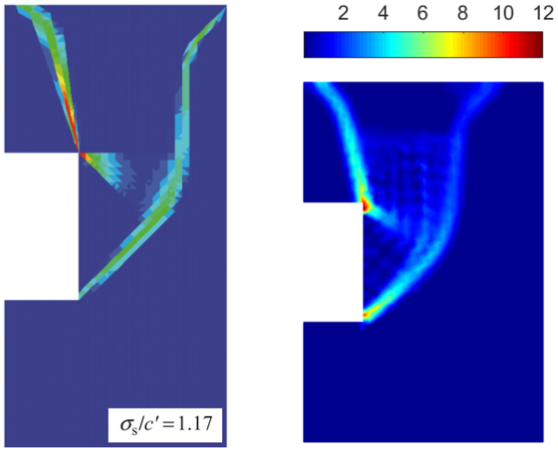

(a) Yamamoto et al. solution [12] (b) SNS-FEM solution

Figure 4. Comparison of power dissipations of a square tunnel in the case $H/B = 1$, $\gamma B/c = 1$, $\phi = 5°$

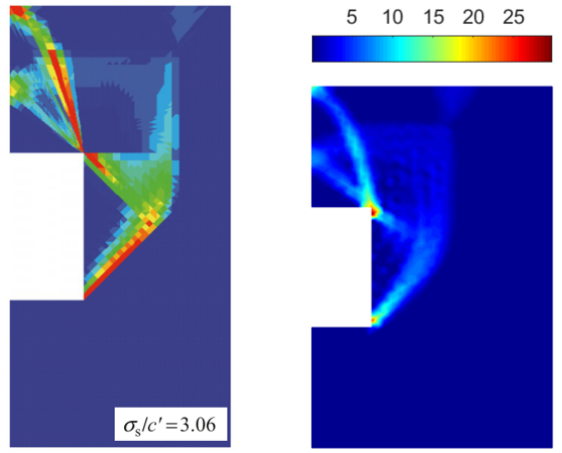

(a) Yamamoto et al. solution [12] (b) SNS-FEM solution

Figure 5. Comparison of power dissipations of a square tunnel in the case $H/B = 1$, $\gamma B/c = 1$, $\phi = 20°$

Figs. 4–5 show the power dissipation of a shallow square tunnel $H/B = 1$ using the SNS-FEM in the case friction angle $\phi = 5°$ and $\phi = 20°$, respectively. Although a different friction angle is used

here, these slip surfaces are almost identical, as seen in Figs. 4(b) and 5(b). The failure mechanism illustrates that a small slip failure occurs in the bottom corner, while a large surface mechanism originates from the top corner of the tunnel and extends up to the ground surface. The slip failures were obtained using the SNS-FEM method presented in Figs. 4(b) and 5(b) are consistent with those reported by Yamamoto et al. [12] in Figs. 4(a) and 5(a).

In the cases of moderate tunnel with $H/B = 2$ and deep tunnel with $H/B = 4$, as shown in Figs. 6(b) and 7(b), the major slip failure mechanisms originate from the bottom corner of the tunnel and extend up to the ground surface. The shapes of failure mechanisms of square tunnels obtained using the SNS-FEM are quite similar to those derived from the FELA approach reported by Yamamoto et al. [12] shown in Figs. 6(a) and 7(a).

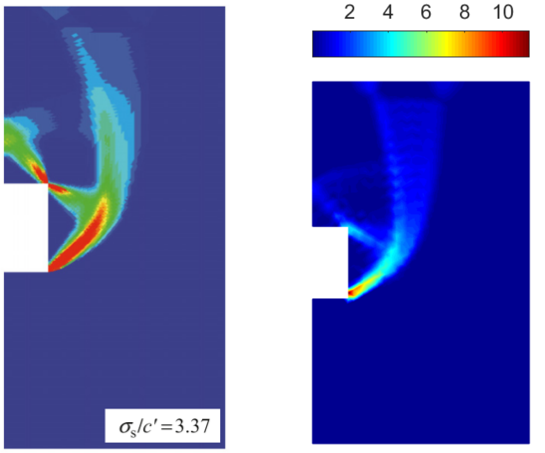

(a) Yamamoto et al. solution [12] (b) SNS-FEM solution

Figure 6. Comparison of power dissipations of a square tunnel in the case $H/B = 2$, $\gamma B/c = 1$, $\phi = 5°$

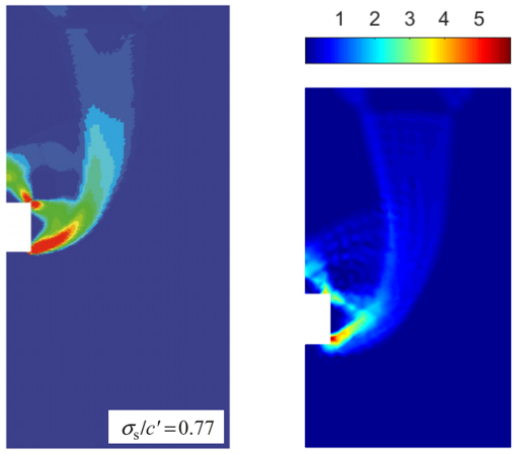

(a) Yamamoto et al. solution [12] (b) SNS-FEM solution

Figure 7. Comparison of power dissipations of a square tunnel in the case $H/B = 4$, $\gamma B/c = 1$, $\phi = 5°$

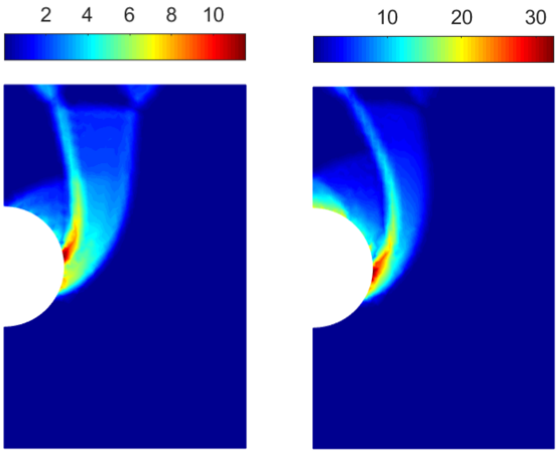

(a) $\phi = 5°$ (b) $\phi = 20°$

Figure 8. Power dissipations of a circular tunnel using the SNS-FEM in the case $H/D = 1$, $\gamma D/c = 1$

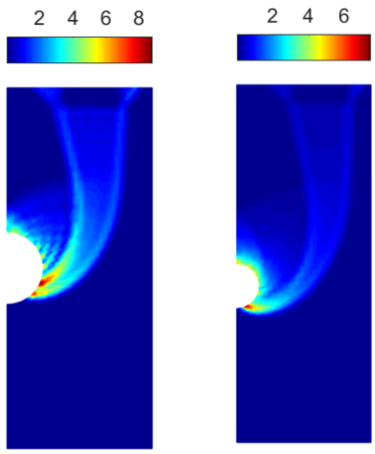

(a) $H/D = 2$ (b) $H/D = 4$

Figure 9. Power dissipations of a circular tunnel using the SNS-FEM in the case $\gamma D/c = 1$, $\phi = 5°$

For comparison, the plots of failure mechanisms of circular tunnels are shown in Figs. 8–9 for the same geometric and soil properties as those presented in Figs. 4–7 for square tunnels. Comparing these plots, it can be observed that the shallow and deep circular tunnel failure mechanisms are quite different from the cases of shallow and deep square tunnels. As expected, the ultimate surcharge loads for circular tunnels are higher than those for square tunnels. It is due to the significant arching effect on stress distribution around a circular tunnel.

Figs. 10–11 show failure mechanisms in the cases of shallow and deep square tunnels with the influence of soil properties $\gamma B/c$. In the case of the shallow tunnel shown in Fig. 10, when $\gamma B/c = 1$, $\gamma B/c = 2.5$, and $\phi = 20°$, the failure mechanisms consist of two parts: (i) a large surface mechanism originates from the top corner of the tunnel and extends up to the ground surface; (ii) a small surface mechanism occurs from the bottom of a square tunnel. Fig. 11 shows the collapse mechanisms of deep tunnels where $\phi = 20°$, $H/B = 4$, $\gamma B/c = 1$, and $\gamma B/c = 2.5$, the failure surfaces around the outer sides of the square tunnels and do not extend to the ground surface. It means that the deep tunnel is more stable when the weight of the soil increases, and the slip surface does not affect the ground surface.

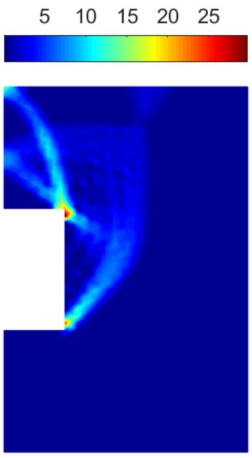

(a) $\gamma B/c = 1$

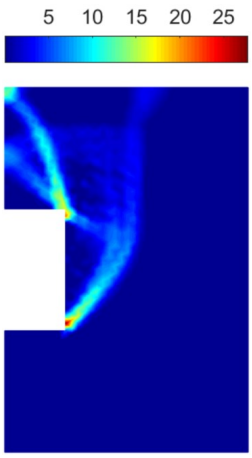

(b) $\gamma B/c = 2.5$

Figure 10. Power dissipations of a square tunnel using the SNS-FEM in the case $H/B = 1$, $\phi = 20°$

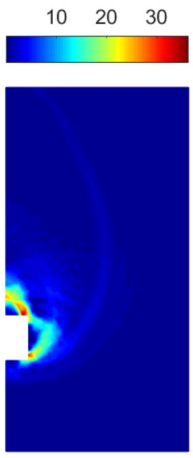

(a) $\gamma B/c = 1$

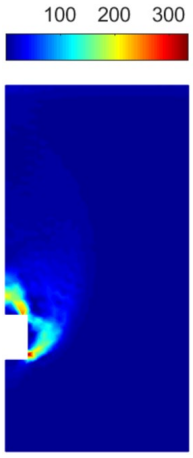

(b) $\gamma B/c = 2.5$

Figure 11. Power dissipations of a square tunnel using the SNS-FEM in the case $H/B = 4$, $\phi = 20°$

4.2. Results of stability numbers

To demonstrate the computational efficiency of the proposed method for stability analysis of a square tunnel, we consider the computational cost based on variables $N_{var,}$ and optimization CPU times are considered for the case $H/B = 1$, $\phi = 30°$, $\gamma B/c = 1$. The reported CPU times only account for the time spent on the interior-point iterations to solve the resulting SOCP problem. Table 1 summarizes the stability numbers σ_s/c, number of variables N_{var}, and CPU times for the finite element limit analysis using triangular elements (FEM-T3), the edge-based smoothed finite element (ES-FEM-T3), and the present approach SNS-FEM. These results highlight the efficiency of the SNS-FEM method in terms of computational cost when compared to other finite element methods for stability analysis of a square tunnel.

Table 1. Comparisons of stability numbers of a square tunnel using the SNS-FEM and other solutions ($H/B = 1$, $\phi = 30°$, $\gamma B/c = 1$, smooth interface)

N_e	FEM-T3			ES-FEM-T3			Present method SNS-FEM		
(T3)	N_{var}	CPU (s)	σ_s/c	N_{var}	CPU (s)	σ_s/c	N_{var}	CPU (s)	σ_s/c
584	2425	0.46	51.12	3433	0.48	34.02	1681	0.44	7.51
918	3783	0.58	27.46	5325	0.61	17.68	2571	0.56	6.91
1668	6821	0.78	16.40	9545	1.05	11.99	4541	0.61	6.78
2256	9195	1.05	14.60	12834	2.20	11.27	6066	0.80	6.76
2640	10743	1.42	14.14	14976	2.69	10.79	7056	0.86	6.75
3796	15405	1.56	13.12	21429	3.98	10.32	10041	1.28	6.74
4764	19301	1.89	11.83	26813	5.49	9.62	12521	1.33	6.71
5312	21509	2.13	11.49	29867	6.20	9.57	13931	1.59	6.68
6014	24335	2.47	11.34	33773	7.50	9.52	15731	1.89	6.68
6860	27733	2.89	11.08	38461	12.83	9.29	17881	2.27	6.68
7898	31907	3.39	10.36	44225	13.25	9.02	20531	2.47	6.68
9226	37241	3.56	10.28	51584	14.92	8.80	23906	2.70	6.67

N_{var}(FEM-T3) = $2N_n + 3N_e$; N_{var}(ES-FEM-T3) = $2N_n + 3N_{ed}$; N_{var}(SNS-FEM) = $5N_n$, where N_{var}, N_n, N_e, and N_{ed} are the number of variables, nodes, triangular elements, and triangular edges in the problems.

Fig. 12 compares the convergence rate archived by the SNS-FEM approach with those of FEM-T3 and ES-FEM-T3. Despite using a coarse mesh, the stability number values obtained using SNS-FEM are more convergent than those obtained using other methods, such as FEM-T3 and ES-FEM-T3. Furthermore, the SNS-FEM approach requires fewer variables than FEM-T3 and ES-FEM-T3 when using the same elements. The optimization problem using SNS-FEM is solved by an interior-point algorithm with fast convergence, requiring only 18 - 23 step iterations with a maximum CPU time of 2.70 s (N_{var} = 23906). This comparison demonstrates the effectiveness of the SNS-FEM approach, which utilizes the Mosek optimizer to solve geotechnical engineering problems.

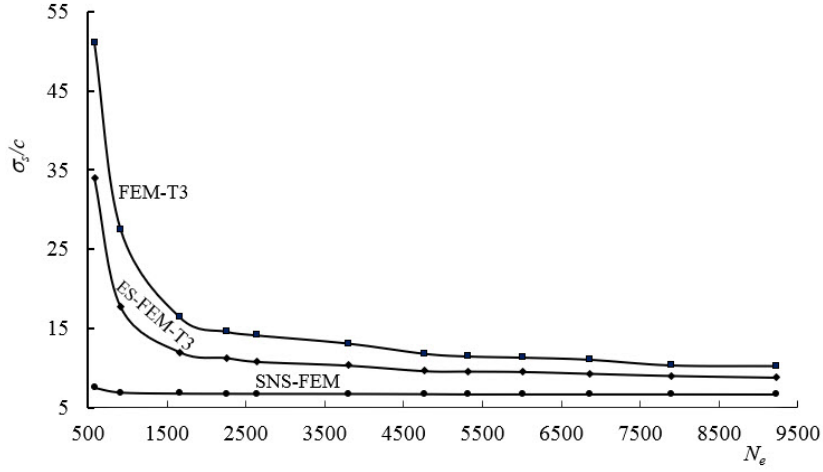

Figure 12. The convergence of stability numbers of a square tunnel $H/B = 1$, $\phi = 30°$, $\gamma B/c = 1$

The SNS-FEM approach is employed to calculate the stability numbers of a square tunnel, and the results are compared with the FELA reported by Yamamoto et al. [12]. It is found that the SNS-FEM method provides an accurate solution, with the majority of the results in good agreement with

the average values of the lower and upper bounds reported by Yamamoto et al. [12]. Furthermore, the SNS-FEM approach required less than 5000 triangular elements to achieve this accuracy, while Yamamoto et al. [12] used 20000 triangular elements and 29850 stress/velocity discontinuities. The errors of the stability numbers from SNS-FEM limit analysis and the average values of the upper and lower bound results reported by Yamamoto et al. [12] are within ± 3%, indicating the reliability and effectiveness of the SNS-FEM method for stability analysis of square tunnels.

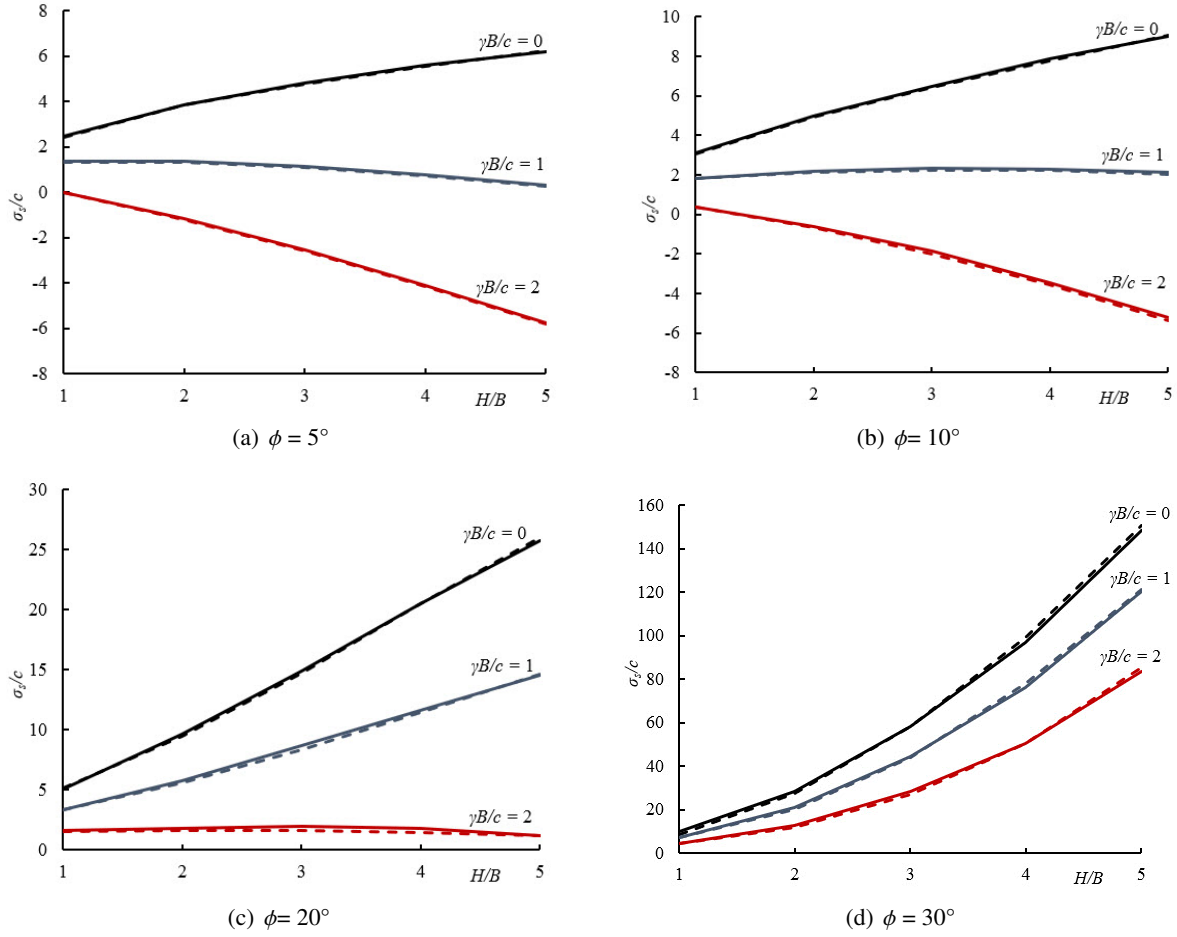

(a) $\phi = 5°$ (b) $\phi = 10°$

(c) $\phi = 20°$ (d) $\phi = 30°$

Figure 13. Comparisons of stability numbers using the SNS-FEM and FELA reported by Yamamoto et al. [12] (smooth interface)

The stability numbers of a square tunnel for various values of $H/B, \phi$ and $\gamma B/c$ are listed in Table 2 for smooth and Table 3 for a rough interface. It is observed that for some cases with H/B ranging from 3 to 5 and $\gamma B/c = 2.5$, the stability numbers σ_s/c are approximately zero, indicating the absence of surcharge loading on the ground surface and the collapse of the tunnels being caused by the unit weight of the soil. It is important to note that the negative stability numbers do not occur in engineering practice, which means that only normal tensile stress can be applied to the ground surface to maintain the stability of the square tunnel. In contrast, positive stability values imply that the square tunnel collapses when subjected to compressive stress on the ground surface.

Table 2. Results of stability numbers σ_s/c (smooth interface)

ϕ	H/B	$\gamma B/c$					
		0	0.5	1	1.5	2	2.5
0	1	1.99	1.47	0.89	0.27	−0.36	−1.00
	2	3.05	1.91	0.75	−0.41	−1.60	−2.79
	3	3.66	2.00	0.37	−1.33	−3.02	−4.73
	4	4.14	1.99	−0.18	−2.36	−4.58	−6.82
	5	4.55	1.89	−0.78	−3.47	−6.20	−8.96
5	1	2.37	1.79	1.17	0.54	−0.11	−0.76
	2	3.77	2.54	1.30	0.05	−1.21	−2.47
	3	4.70	2.88	1.07	−0.75	−2.58	−4.43
	4	5.48	3.10	0.70	−1.70	−4.12	−6.56
	5	6.16	3.20	0.22	−2.77	−5.79	−8.85
10	1	2.89	2.24	1.59	0.92	0.23	−0.47
	2	4.82	3.46	2.08	0.71	−0.67	−2.07
	3	6.31	4.28	2.25	0.17	−1.95	−4.07
	4	7.67	4.95	2.19	−0.61	−3.48	-
	5	8.89	5.48	1.99	−1.56	−5.28	-
15	1	3.61	2.88	2.15	1.43	0.67	−0.08
	2	6.44	4.89	3.28	1.75	0.16	−1.45
	3	9.06	6.66	4.22	1.75	−0.80	−3.41
	4	11.62	8.37	5.20	1.56	−2.09	-
	5	13.97	9.88	5.58	1.06	-	-
20	1	4.67	3.84	3.01	2.17	1.32	0.47
	2	9.21	7.35	5.47	3.55	1.61	−0.37
	3	14.27	11.30	8.19	5.04	1.70	−1.74
	4	19.44	15.37	11.03	6.43	1.45	-
	5	24.62	19.43	13.80	7.74	0.88	-
25	1	6.36	5.38	4.39	3.39	2.37	1.34
	2	14.51	12.10	9.65	7.15	4.57	1.91
	3	25.53	21.60	17.13	12.77	7.86	2.93
	4	37.77	32.14	25.99	19.28	11.81	3.57
	5	51.77	44.56	36.47	27.40	17.31	3.47
30	1	9.22	8.00	6.76	5.51	4.22	2.90
	2	26.33	22.87	19.28	15.57	11.71	7.67
	3	54.08	48.68	41.50	34.37	26.16	17.62
	4	89.04	80.11	70.05	58.66	45.82	31.14
	5	137.04	125.14	111.57	96.04	78.26	48.82
35	1	14.64	12.99	11.31	9.59	7.84	6.01
	2	58.66	52.70	46.22	39.57	32.54	24.98
	3	147.41	138.64	124.00	110.31	93.54	74.24
	4	289.90	270.64	248.34	222.80	193.45	158.83
	5	509.54	483.71	452.44	415.87	373.43	323.68

Table 3. Results of stability numbers σ_s/c (rough interface)

ϕ	H/B	$\gamma B/c$					
		0	0.5	1	1.5	2	2.5
0	1	2.04	1.54	0.94	0.16	−0.31	−1.31
	2	3.12	1.97	0.82	−0.35	−1.54	−2.73
	3	3.73	2.07	0.41	−1.26	−2.97	−4.78
	4	4.16	2.04	−0.35	−2.30	−4.94	−6.91
	5	4.59	1.74	−1.01	−3.79	−6.59	−9.42
5	1	2.47	1.93	1.39	0.70	−0.01	−0.72
	2	3.87	2.63	1.38	0.12	−1.15	−2.41
	3	4.81	2.98	1.16	−0.67	−2.53	−4.38
	4	5.58	3.18	0.77	−1.65	−4.09	−6.54
	5	6.21	3.28	0.30	−2.72	−5.75	−8.83
10	1	3.11	2.49	1.84	1.12	0.38	−0.34
	2	4.96	3.59	2.20	0.81	−0.59	−1.99
	3	6.49	4.43	2.35	0.25	−1.86	−4.01
	4	7.85	5.08	2.29	−0.54	−3.44	-
	5	9.01	5.66	2.13	−1.45	−5.24	-
15	1	4.01	3.24	2.45	1.68	0.89	0.09
	2	6.68	5.11	3.51	1.91	0.20	−1.34
	3	9.39	6.94	4.46	1.94	−0.64	−3.34
	4	12.01	8.65	5.23	1.69	−1.99	-
	5	14.21	10.30	5.87	1.32	−1.72	-
20	1	5.11	4.24	3.37	2.48	1.60	0.70
	2	9.64	7.73	5.80	3.84	1.83	−0.19
	3	14.93	11.84	8.67	5.40	1.99	−1.61
	4	20.47	16.14	11.64	6.85	1.81	-
	5	25.73	20.51	14.54	8.44	1.22	-
25	1	6.84	5.82	4.79	3.75	2.70	1.64
	2	15.37	12.82	10.35	7.71	5.06	2.27
	3	27.01	22.76	18.26	13.56	8.63	3.33
	4	40.23	34.32	27.83	20.58	12.93	4.15
	5	54.05	47.15	37.88	29.27	17.62	5.87
30	1	9.85	8.57	7.28	5.97	4.64	3.28
	2	28.33	24.41	20.96	16.82	12.97	8.53
	3	58.08	51.68	44.52	36.77	28.38	19.37
	4	97.07	87.62	76.42	64.49	50.64	35.03
	5	148.47	135.34	120.26	102.99	83.43	60.42
35	1	15.82	14.06	12.27	10.44	8.57	6.63
	2	64.35	56.69	51.33	42.99	36.72	27.57
	3	160.58	148.69	135.66	120.34	103.19	83.82
	4	319.03	298.53	273.07	246.28	213.55	177.39
	5	570.78	539.46	502.04	458.19	407.05	347.28

Figs. 13–14 show the variation of the stability numbers σ_s/c with H/B from 1 to 5 and different friction angle values ϕ ranging from 5° to 30° in smooth and rough interfaces, respectively. The results obtained from the present method exhibit a slightly higher value than the solution presented by Yamamoto et al. [12]. When considering weightless soil $\gamma B/c = 0$, the square tunnel stability σ_s/c with an increasing H/B for all friction angles ϕ. However, when $\sigma_s/c = 2$ and $\phi < 20°$, an increase in the value of H/B leads to a decrease in the stability numbers. Conversely, when $\gamma B/c = 2$ and $\phi \geq 20°$, the stability numbers increase continuously with an increase in H/B. These findings indicate that the internal friction angle ϕ of the soil significantly influences the results of surcharge loading when its values increase.

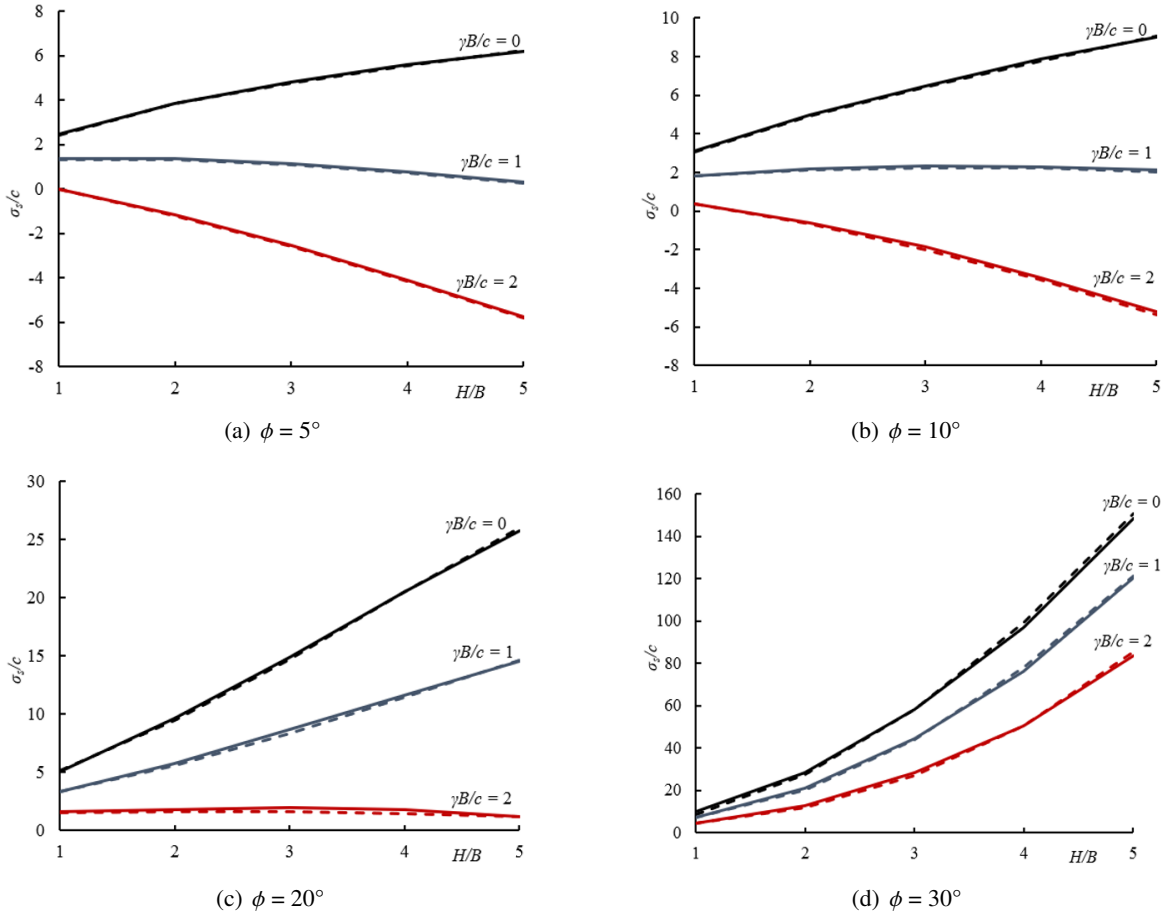

Figure 14. Comparisons of stability numbers using the SNS-FEM and FELA reported by Yamamoto et al. [12] (rough interface)

Fig. 15 illustrates the variation of the stability numbers for different values of ϕ and $\gamma B/c$ in the case $H/B = 1$ and $H/B = 3$ (smooth interface). It is important to note that, for given values of H/B and ϕ, the stability numbers demonstrate decreases as the soil weight $\gamma B/c$ increases. In contrast, for a given value of $\gamma B/c$, the stability numbers increase continuously with an increase in the friction angle of soil ϕ. For the case with a rough interface condition, the stability numbers are almost the same as for the smooth case, but the collapse loads σ_s/c are slightly higher.

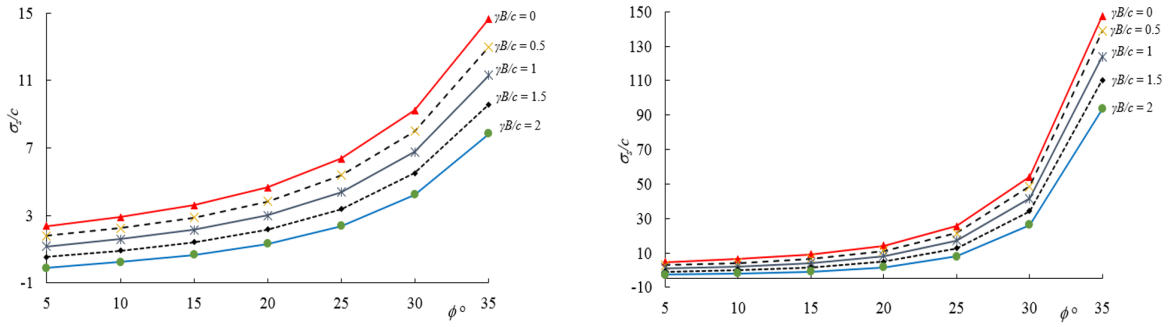

(a) $H/B = 1$ (smooth interface) (b) $H/B = 3$ (smooth interface)

Figure 15. Variation of the stability numbers σ_s/c for different values of ϕ and $\gamma B/c$

5. Conclusions

This research paper introduces the utilization of the upper bound theorem in combination with a stable node-based smoothed finite element (SNS-FEM) and the second-order cone programming (SOCP) to investigate the effect of surcharge loading on a square tunnel stability analysis in cohesive-frictional soils. Design tables and dimensionless charts with various soil properties $\gamma B/c$ and ϕ, geometric parameters H/B are presented. The following conclusions can be drawn:

- The stability numbers value σ_s/c for all friction angles decreases with an increase in soil property $\gamma B/c$. In contrast, the magnitudes of stability results show a continuous increase with an increase in both H/B and ϕ.

- For shallow square tunnels, the failure mechanism illustrates that a small slip failure occurs in the bottom corner, while a large surface mechanism originates from the top corner of the tunnel and extends up to the ground surface. For medium and deep tunnels, the major slip failure mechanisms originate from the bottom corner of the tunnel and extend up to the ground surface.

- The numerical results are available for the cases of $\phi \leq 35°$, allowing geotechnical engineers to utilize them in the preliminary design stage of square tunnels. The proposed method is highly robust and easily extendable for analyzing stability in various geotechnical engineering problems.

Acknowledgments

The author would like to thank the Foundation for Science and Technology for support at HUTECH University. This support is gratefully acknowledged.

References

[1] Cairncross, A. M. (1973). Deformations around model tunnels in stiff clay. PhD thesis, University of Cambridge, UK.

[2] Atkinson, J. H., Potts, D. M. (1977). Stability of a shallow circular tunnel in cohesionless soil. *Géotechnique*, 27(2):203–215.

[3] Seneviratne, H. N. (1979). Deformations and pore-pressures around model tunnels in soft clay. PhD thesis, University of Cambridge, UK.

[4] Davis, E. H., Gunn, M. J., Mair, R. J., Seneviratine, H. N. (1980). The stability of shallow tunnels and underground openings in cohesive material. *Géotechnique*, 30(4):397–416.

[5] Mühlhaus, H. B. (1985). Lower bound solutions for circular tunnels in two and three dimensions. *Rock Mechanics and Rock Engineering*, 18(1):37–52.

[6] Leca, E., Dormieux, L. (1990). Upper and lower bound solutions for the face stability of shallow circular tunnels in frictional material. *Géotechnique*, 40(4):581–606.

[7] Sloan, S. W., Assadi, A. (1991). Undrained stability of a square tunnel in a soil whose strength increases linearly with depth. *Computers and Geotechnics*, 12(4):321–346.

[8] Lyamin, A. V., Sloan, S. W. (2000). Stability of a plane strain circular tunnel in a cohesive frictional soil. In *Proceedings of the J.R. Booker Memorial Symposium, Sydney*, 139–153.

[9] Lyamin, A. V., Jack, D. L., Sloan, S. W. (2001). Collapse Analysis of Square Tunnels in Cohesive–Frictional Soils. In *Computational Mechanics–New Frontiers for the New Millennium*, Elsevier, 405–414.

[10] Yang, F., Yang, J. S. (2010). Stability of Shallow Tunnel Using Rigid Blocks and Finite-Element Upper Bound Solutions. *International Journal of Geomechanics*, 10(6):242–247.

[11] Yamamoto, K., Lyamin, A. V., Wilson, D. W., Sloan, S. W., Abbo, A. J. (2011). Stability of a circular tunnel in cohesive-frictional soil subjected to surcharge loading. *Computers and Geotechnics*, 38(4): 504–514.

[12] Yamamoto, K., Lyamin, A. V., Wilson, D. W., Sloan, S. W., Abbo, A. J. (2011). Stability of a single tunnel in cohesive–frictional soil subjected to surcharge loading. *Canadian Geotechnical Journal*, 48 (12):1841–1854.

[13] Vo-Minh, T., Nguyen-Son, L., Nguyen-Van, G., Thai-Phuong, T. (2021). Upper bound limit analysis of circular tunnel in cohesive-frictional soils using isogeometric analysis based on Bézier extraction. *Tunnelling and Underground Space Technology*, 114:103995.

[14] Liu, G. R., Nguyen-Thoi, T., Nguyen-Xuan, H., Lam, K. Y. (2009). A node-based smoothed finite element method (NS-FEM) for upper bound solutions to solid mechanics problems. *Computers & Structures*, 87 (1–2):14–26.

[15] Nguyen-Thoi, T., Liu, G. R., Nguyen-Xuan, H. (2009). Additional properties of the node-based smoothed finite element method (NS-FEM) for solid mechanics problems. *International Journal of Computational Methods*, 06(04):633–666.

[16] Nguyen-Thoi, T., Vu-Do, H. C., Rabczuk, T., Nguyen-Xuan, H. (2010). A node-based smoothed finite element method (NS-FEM) for upper bound solution to visco-elastoplastic analyses of solids using triangular and tetrahedral meshes. *Computer Methods in Applied Mechanics and Engineering*, 199(45–48): 3005–3027.

[17] Nguyen-Xuan, H., Rabczuk, T., Nguyen-Thoi, T., Tran, T. N., Nguyen-Thanh, N. (2011). Computation of limit and shakedown loads using a node-based smoothed finite element method. *International Journal for Numerical Methods in Engineering*, 90(3):287–310.

[18] Vo-Minh, T., Nguyen-Minh, T., Chau-Ngoc, A. (2018). Upper Bound Limit Analysis of Circular Tunnel in Cohesive-Frictional Soils Using the Node-Based Smoothed Finite Element Method. In *Lecture Notes in Mechanical Engineering*, Springer Singapore, 123–141.

[19] Vo, T. M., Nguyen, T. M., Chau, A. N., Nguyen, H. C. (2017). Stability of twin circular tunnels in cohesive-frictional soil using the node-based smoothed finite element method (NS-FEM). *Journal of Vibroengineering*, 19(1):520–538.

[20] Vo, T.-M., Chau, A.-N., Nguyen, T.-M., Nguyen, H.-C. (2018). A node-based smoothed finite element method for stability analysis of dual square tunnels in cohesive-frictional soils. *Scientia Iranica*, 25(3): 1105–1121.

[21] Vo-Minh, T. (2023). The Upper bound limit analysis of slope in cohesive-frictional soils using the node-based smoothed finite element method. *Journal of Science and Technology in Civil Engineering (STCE) - HUCE*, 17(3):140–153.

[22] Liu, G. R., Chen, L., Nguyen-Thoi, T., Zeng, K. Y., Zhang, G. Y. (2010). A novel singular node-based smoothed finite element method (NS-FEM) for upper bound solutions of fracture problems. *International Journal for Numerical Methods in Engineering*, 83(11):1466–1497.

[23] Xu, X., Gu, Y., Liu, G. (2013). A hybrid smoothed finite element method (H-SFEM) to solid mechanics problems. *International Journal of Computational Methods*, 10(01):1340011.

[24] Wang, G., Cui, X. Y., Feng, H., Li, G. Y. (2015). A stable node-based smoothed finite element method for acoustic problems. *Computer Methods in Applied Mechanics and Engineering*, 297:348–370.

[25] Feng, H., Cui, X. Y., Li, G. Y. (2016). A stable nodal integration method with strain gradient for static

and dynamic analysis of solid mechanics. *Engineering Analysis with Boundary Elements*, 62:78–92.

[26] Yang, H., Cui, X. Y., Li, S., Bie, Y. H. (2018). A stable node-based smoothed finite element method for metal forming analysis. *Computational Mechanics*, 63(6):1147–1164.

[27] Vo-Minh, T., Nguyen-Son, L. (2021). A stable node-based smoothed finite element method for stability analysis of two circular tunnels at different depths in cohesive-frictional soils. *Computers and Geotechnics*, 129:103865.

[28] Vo-Minh, T., Nguyen, H. C. (2022). Seismic stability of a circular tunnel in cohesive-frictional soils using a stable node-based smoothed finite element method. *Tunnelling and Underground Space Technology*, 130:104606.

[29] Vo-Minh, T., Nguyen-Son, L., Anh Nguyen, T. (2023). Stable node-based smoothed finite element method for seismic stability analysis of a square tunnel in cohesive-frictional soils. *Tunnelling and Underground Space Technology*, 141:105346.

[30] Mosek. *The MOSEK optimization toolbox for MATLAB manual*.

[31] Makrodimopoulos, A., Martin, C. M. (2006). Upper bound limit analysis using simplex strain elements and second-order cone programming. *International Journal for Numerical and Analytical Methods in Geomechanics*, 31(6):835–865.

[32] GiD 11.0.4. *International Center for Numerical Methods in Engineering (CIMNE)*. Reference manual.